



Article

Insights into the Electrocatalytic Activity of Fe,N-Glucose/Carbon Nanotube Hybrids for the Oxygen Reduction Reaction

Rafael G. Morais ^{1,2,*}, Natalia Rey-Raap ³, José L. Figueiredo ^{1,2} and Manuel F. R. Pereira ^{1,2,*}

- ¹ LSRE-LCM—Laboratory of Separation and Reaction Engineering—Laboratory of Catalysis and Materials, Faculty of Engineering, University of Porto, Rua Dr. Roberto Frias, 4200-465 Porto, Portugal; jlfig@fe.up.pt
- ² ALiCE—Associate Laboratory in Chemical Engineering, Faculty of Engineering, University of Porto, Rua Dr. Roberto Frias, 4200-465 Porto, Portugal
- ³ Instituto de Ciencia y Tecnología del Carbono, INCAR-CSIC, Francisco Pintado Fe 26, 33011 Oviedo, Spain; natalia.rey@incar.csic.es
- * Correspondence: rgm@fe.up.pt (R.G.M.); fpereira@fe.up.pt (M.F.R.P.)

Abstract: Glucose-derived carbon hybrids were synthesized by hydrothermal treatment in the presence of oxidized carbon nanotubes. Additionally, iron and nitrogen functionalities were incorporated into the carbon structure using different methodologies. The introduction of iron and nitrogen in a single step under a H₂ atmosphere favored the formation of quaternary nitrogen and oxidized nitrogen, whereas the incorporation of nitrogen under an N₂ atmosphere after doping the hybrids with iron mainly produced pyridinic nitrogen. The samples were characterized by scanning electron microscopy, X-ray spectroscopy, adsorption isotherms, inductively coupled plasma optical emission spectrometry, and Raman spectroscopy. The presence of iron and nitrogen in the carbons increases the onset potential toward oxygen reduction in KOH 0.1 mol L⁻¹ by 130 mV (0.83 V), in comparison to carbonized glucose, whereas the reaction mechanism shifts closer to a direct pathway and the formation of HO₂⁻ decreases to 25% (3.5 electrons). The reaction rate also increased in comparison to the carbonized glucose, as observed by the decrease in the Tafel slope value from 117 to 61 mV dec⁻¹. Furthermore, the incorporation of iron and nitrogen in a single step enhanced the short-term performance of the prepared electrocatalysts, which may also be due to the higher relative amount of quaternary nitrogen.

Keywords: carbon-based electrocatalyst; carbon nanotubes; oxygen reduction reaction; nitrogen-doping; iron



Citation: Morais, R.G.; Rey-Raap, N.; Figueiredo, J.L.; Pereira, M.F.R. Insights into the Electrocatalytic Activity of Fe,N-Glucose/Carbon Nanotube Hybrids for the Oxygen Reduction Reaction. *C* **2024**, *10*, 47. <https://doi.org/10.3390/c10020047>

Academic Editors: Nikolaos Kostoglou and Claus Rebholz

Received: 15 April 2024
Revised: 2 May 2024
Accepted: 14 May 2024
Published: 17 May 2024



Copyright: © 2024 by the authors. Licensee MDPI, Basel, Switzerland. This article is an open access article distributed under the terms and conditions of the Creative Commons Attribution (CC BY) license (<https://creativecommons.org/licenses/by/4.0/>).

1. Introduction

Fuel cells represent one of the most promising alternatives to fossil fuels for sustainable green electrical energy conversion due to the low emission of pollutants, high efficiency, and non-polluting reaction products [1,2]. However, the oxygen reduction reaction (ORR) that takes place at the cathode presents highly sluggish kinetics and hinders the overall device operation [2–9]. Platinum-based electrocatalysts are the most commonly used to supply faster kinetics [3,5,6,8,10–14]. However, Pt is a scarce and expensive noble metal, contributing to the high costs associated with fuel cell production [15]. Consequently, the growing need to optimize green energy conversion devices has led to ever-increasing efforts to design non-noble metal electrocatalysts that display high electroactivity toward ORR and long-term durability.

The high versatility and lower price of carbon materials in comparison with metal-based materials make them one of the most interesting supports for electrocatalysts [2,16,17]. The modification of the physical and chemical properties of carbons can result in materials with higher electroactivity, which is essential for the ORR. In order to preserve the ecological

friendliness of carbon materials, the combination of a green carbon source and an adequate synthesis method is essential. The use of biomass and hydrothermal carbonization (HTC) are presented as two interesting strategies for the abovementioned objective. Biomass is one of the most abundant carbon sources in the world and presents a relatively low cost. Furthermore, HTC is a low-cost methodology to obtain biomass-derived carbons using mild operating conditions via an environmentally friendly process [18–22]. This combination results in spherical particles that usually display low porosity and low electroactivity toward the ORR [19–22]. To overcome this drawback, tailoring the properties of carbons obtained by HTC is necessary. Carbonization and activation methods are usually employed to develop porosity, while the chemical properties can be modified by the incorporation of heteroatoms and/or transition metals. Nitrogen is considered the most effective heteroatom to enhance the carbon electrocatalyst's activity toward the ORR [19,21–26]. The presence of pyridinic nitrogen is important for O₂ bonding, whereas the incorporation of quaternary nitrogen favors oxygen dissociation [20]. Additionally, carbon nanotubes (CNTs) can also be added during the polymerization of glucose to increase the degree of polymerization and lower the surface's acidity and the graphitization level of the HTC carbons, in order to enhance the electron transfer kinetics during the ORR [19,22,27]. Nonetheless, the obtained electroactivities are still inferior to those of benchmark catalysts, and the incorporation of transition metals is essential to enhance the catalytic activity of these hybrids. Among transition metals, iron is largely reported to give rise to high performances toward the ORR [28,29], and the synergy between nitrogen and iron is one of the most important features in the reduction of oxygen and has been reported to achieve outstanding performances [30–34]. However, the effect of nitrogen and iron on carbon materials and their synergy largely depends on the structure and morphology of the supports [35] and the methodology employed for their incorporation [28]. Therefore, this work aims to shed light on the synergistic effect between nitrogen and iron incorporated by different methodologies and to evaluate which are the most promising for obtaining electrocatalysts with high efficiency and electroactivity toward the ORR. Accordingly, this work studies the effect of a wide range of iron concentrations added to carbonized glucose (CG). Additionally, the effect of the incorporation of a selected amount of iron on both CG and CG/CNT hybrids was studied, determining the influence of CNTs on the single incorporation of the transition metal. The effect of the methodology employed to introduce nitrogen to the CG and hybrids has also been assessed by following two different pathways to achieve Fe,N carbon samples: (i) a two-step method featuring the incorporation of iron oxide, followed by its reduction and the subsequent impregnation of melamine, as well as its decomposition into nitrogen functionalities by employing a thermal treatment under an inert atmosphere, or (ii) a one-step method featuring the impregnation of iron oxide and melamine followed by thermal treatment under a H₂ atmosphere. These methodologies allow us to understand how nitrogen functionalities are affected by the process and the base carbon employed (CG or hybrid), and, hence, the electroactivity toward the ORR.

2. Materials and Methods

2.1. Reagents

D(+)-Glucose (HiMedia, Modautal, Germany, >99%), distilled water (produced on-site in a distillation unit), multiwalled CNT (Nanocyl, Sambreville, Belgium, C > 95%), and nitric acid (HNO₃, Honeywell, Charlotte, NC, USA ≥65%) were used to prepare the carbon materials. Fe₂O₃ (Sigma-Aldrich, St. Louis, MO, USA, ≥99%) and melamine (C₃H₆N₆, Sigma-Aldrich, 99%) were employed to functionalize the carbon supports. All gases used throughout this work were supplied by Air Liquide (Paris, France): nitrogen (N₂, 99.999%), hydrogen (H₂, 99.999%), and oxygen (O₂, 99.995%) were used during thermal treatments and/or electrochemical assessments. Nafion (Sigma-Aldrich, 5 wt.% in a mixture of water (15–20%) and aliphatic alcohols), absolute ethanol (VWR Chemicals, Radnor, PA, USA), and ultrapure water, produced by inverse osmosis using Panice equipment, were used for the preparation of the electrocatalysts' dispersion, whereas methanol (VWR Chemicals, Radnor,

PA, USA, $\geq 99.9\%$) was employed during methanol tolerance measurements. Platinum on carbon black (Pt/C, Alfa-Aesar, Haverrill, MA, USA, platinum nominal 20% on carbon black) was used as the ORR benchmark catalyst.

2.2. Preparation of Electrocatalysts

Glucose-derived carbon materials were prepared through the hydrothermal polymerization of glucose. Briefly, glucose (15.0 wt.%) was dispersed under sonication in distilled water (85.0 wt.%) for 30 min in a Teflon-lined reactor chamber. Afterward, the solution was closed in a Teflon-lined stainless-steel autoclave and underwent hydrothermal processing at 180 °C for 12 h. The resulting organic polymer was then abundantly washed with distilled water, filtered at room temperature, and dried at 100 °C for 16 h. The material was then carbonized under an N₂ atmosphere for 2 h at 800 °C using a heating ramp of 10 °C min⁻¹.

The chemical composition of the carbonized glucose sample was then modified by incorporating iron or iron/nitrogen according to three different methodologies, as detailed in Figure 1: (i) different amounts of Fe₂O₃ were impregnated into the carbonized material by incipient wetness impregnation and treated under an N₂ atmosphere for 2 h, then under a H₂ atmosphere for an additional 2 h at 650 °C, to achieve a certain final wt.% of iron on the carbon sample (0.5 wt.%, 1 wt.% or 5 wt.%, samples CG_{0.5Fe}, CG_{1Fe} and CG_{5Fe}, respectively); (ii) the prepared CG_{5Fe} sample was mixed with melamine in a 2:3 melamine/CG ratio, followed by thermal treatment at 650 °C in an N₂ atmosphere for 2 h (two-step method, sample N-CG_{5Fe}), and (iii) the simultaneous incorporation of 5 wt.% of iron oxide and melamine in a 2:3 melamine/CG ratio followed by a single thermal treatment, first in N₂ (2 h) and then under a H₂ atmosphere (2 h) at 650 °C (one-step method, sample CG_{5Fe,N}). All treatments were performed with a gas flow rate of 150 cm³ min⁻¹ and a heating rate of 10 °C min⁻¹.

Additionally, a series of hybrids were prepared by adding oxidized carbon nanotubes (CNT_O) during the hydrothermal polymerization of glucose, as described elsewhere [19]. A typical liquid-phase oxidation method was employed to obtain CNT_O. Briefly, a 7 mol L⁻¹ solution of HNO₃ was used to oxidize CNTs for 3 h at the boiling temperature using a ratio of 75 mL of nitric acid per g of CNTs. The resulting oxidized material was then abundantly washed with distilled water until the water pH was attained and subsequently dried for 24 h at 80 °C. The hydrothermal hybrid was prepared following the same hydrothermal treatment procedure as that employed for the CG sample but using 14.7 wt.% of glucose, 0.3 wt.% of CNT_O, and 85.0 wt.% of distilled water as the initial dispersion. The resulting hydrothermal hybrid was carbonized under an inert atmosphere for 2 h at 800 °C and labeled CG/CNT_O. Afterward, the chemical composition of the material was also modified, as detailed in Figure 1. Fe₂O₃ was incorporated into CG/CNT_O by incipient wetness impregnation, followed by thermal treatment in N₂ (2 h) and then in H₂ atmosphere (2 h) at 650 °C to achieve a final iron content of 5 wt.% (CG/CNT_{O,5Fe}). Moreover, CG/CNT_{O,5Fe} was mixed with melamine in a 2:3 melamine/CG/CNT_O ratio followed by the same thermal treatment as sample N-CG_{5Fe} (two-step method, N-CG/CNT_{O,5Fe}). Lastly, iron and nitrogen were simultaneously incorporated into CG/CNT_O following the same methodology as that used to prepare CG_{5Fe,N} (one-step method, CG/CNT_{O,5Fe,N}).

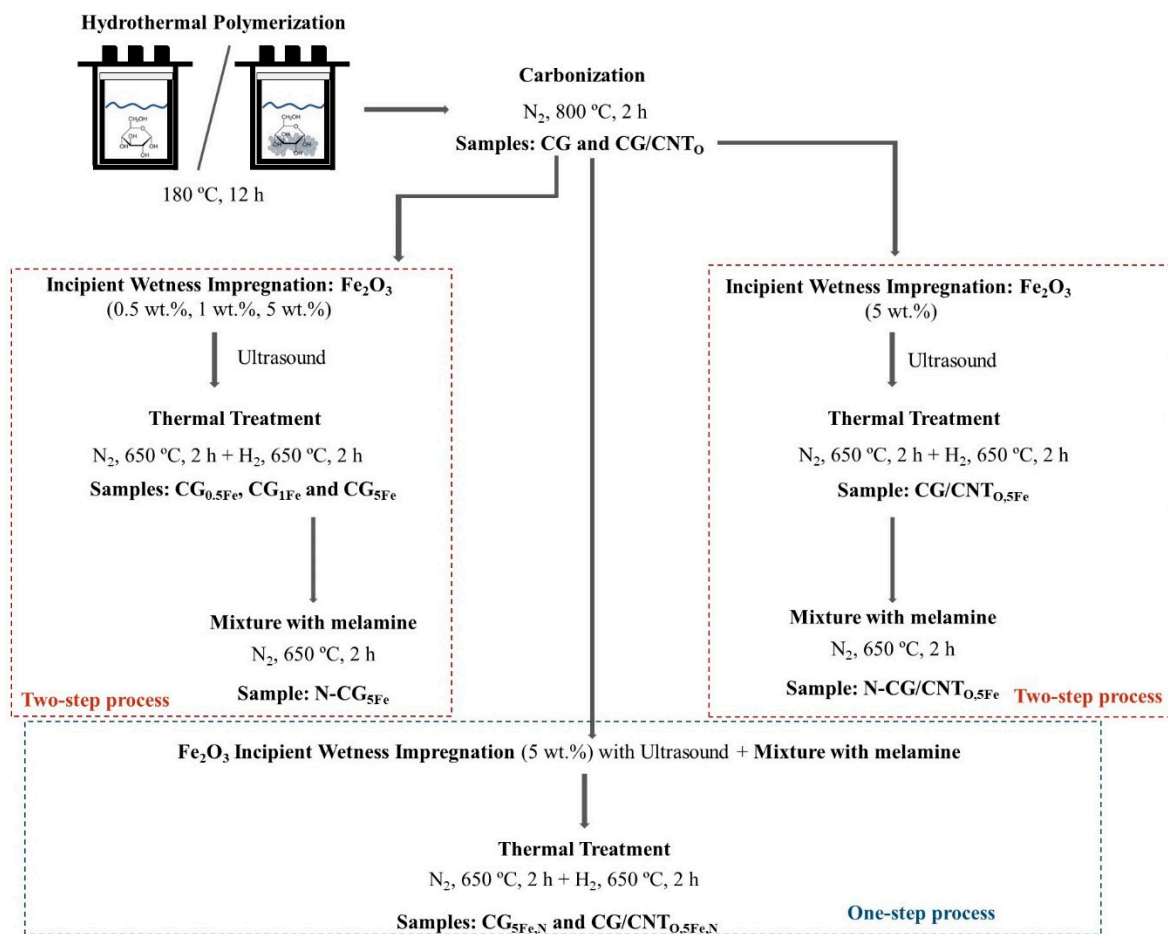


Figure 1. Scheme of the synthesis methodologies employed to prepare Fe,N carbon electrocatalysts.

2.3. Chemical and Textural Characterization

The contents of carbon, hydrogen, and nitrogen (C, H, and N) in the electrocatalysts were assessed by combusting the sample at 1050 °C using a Vario Micro Cube analyzer (Elementar GmbH, Langensfeld, Germany), whereas the oxygen content was measured by pyrolyzing the sample at 1450 °C in a Rapid Oxy Cube analyzer (Elementar GmbH, Langensfeld, Germany). To ensure the homogeneity and reproducibility of all results, triplicate analyses were performed for each material. To further understand the full composition of the prepared carbons, a Perkin Elmer Optima 4300 spectrometer (PerkinElmer, Waltham, MA, USA) was used to perform inductively coupled plasma optical emission spectrometry (ICP-OES) analyses to quantify the iron loading of Fe-CG and Fe-CG/CNT_O samples. This spectrometer was composed of an Echelle polychromator optic. To comprehend the chemical surface composition of each sample, a Kratos AXIS Ultra HAS spectrometer was used to perform X-ray photoelectron spectroscopy (XPS). The analyses were carried out in fixed analyzer transmission mode at 14 kV (175 W) using monochromatic radiation (Al K α , 1486.7 eV). Regarding the textural properties, N₂ adsorption–desorption isotherms at –196 °C were obtained for each carbon material using an automated gas sorption analyzer (Autosorb iQ, Quantachrome, Boynton Beach, FL, USA). Before the analysis, all samples underwent degasification for 12 h at 150 °C. The specific surface area (S_{BET}) was calculated using the Brunauer–Emmett–Teller (BET) equation, whereas the volume of nitrogen adsorbed at a relative pressure of 0.99 (saturation point) was used to calculate the total pore volume (V_{p}). The microporous volume (V_{micro}) was determined by the t -plot method. All samples were analyzed by scanning electron microscopy (SEM) to observe their morphology, and the Fe,N hybrids were also analyzed by elemental map distribution. These analyses were performed in a Nova NanoSEM 200 (FEI Company, Hillsboro, OR,

USA). A conductive carbon double-sided adhesive tape was used to attach the powders of each sample onto an aluminum pin. During SEM analyses, an Everhart–Thornley detector (ETD) was used. Regarding elemental mapping, an Si(Li) detector was employed. Raman spectroscopy was performed using a monochromatic wavelength laser of 532 nm in an Alpha 300 apparatus (WiTec, Ulm, Germany), by directly measuring the spectra on the carbons.

2.4. Electrochemical Characterization

The synthesized electrocatalysts were electrochemically characterized using a PGSTAT 302 N potentiostat/galvanostat and a three-electrode beaker-type cell. The reference and counter electrodes used in this system were Ag/AgCl (KCl 3 mol L⁻¹) and a glassy carbon rod, respectively. A rotating ring-disk electrode (RRDE, Metrohm, Herisau, Switzerland, 24.9% collection efficiency, 5 mm in diameter) composed of a glassy carbon disk and a Pt ring was used as a working electrode for linear sweep voltammetry (LSV) and cyclic voltammetry (CV) assessments. Additionally, a rotating disk electrode (RDE, Metrohm, Herisau, Switzerland, 3 mm in diameter) also consisting of a glassy carbon disk was used as the working electrode to perform chronoamperometric measurements. These electrodes were prepared by drop-casting a suspension containing the carbon electrocatalysts to achieve a final mass loading of ca. 0.27 mg cm⁻². The suspension was prepared by mixing 4 mg of the electrocatalyst, 470 µL of ultrapure water (Millipore, Burlington, MA, USA), 80 µL of Nafion (5 wt% in lower aliphatic alcohols and water, Sigma-Aldrich, St. Louis, MO, USA), and 80 µL of ethanol (≥99.5%, VWR Chemicals, Radnor, PA, USA). Before drop casting, the suspension underwent sonication for at least 30 min until homogeneity was achieved.

The ORR activity was initially analyzed by LSV and CV measurements, which were performed in N₂-saturated 0.1 mol L⁻¹ KOH followed by experiments in O₂-saturated electrolytes. The potentials applied during the electrochemical measurements were corrected to reversible hydrogen electrode (RHE) potentials by applying the following equation:

$$E(\text{RHE}) = E\left(\frac{\text{Ag}}{\text{AgCl}}\right) + E^0\left(\frac{\text{Ag}}{\text{AgCl}}\right) + 0.059\text{pH} = 0.964\text{V}, \quad (1)$$

where $E(\text{RHE})$ is the potential corrected to the RHE, $E(\text{Ag}/\text{AgCl})$ is the potential applied to the reference electrode, and $E^0(\text{Ag}/\text{AgCl})$ is the potential difference between the Ag/AgCl (3 mol L⁻¹) electrode and the RHE (0.197 V).

An initial screening of redox reactions that could take place under the inert medium was accomplished by CV using a scan rate that ranged from 5 to 100 mV s⁻¹ with no rotation. Afterward, LSVs were performed by rotating the working electrode from 400 to 3000 rpm and using a scan rate of 5 mV s⁻¹. Both measurements were performed from 1.15 V to -0.05 V (vs RHE). The O₂-saturated assessments were performed using the same procedure after completion of the experiments in the N₂-saturated electrolyte. The experimental current densities were obtained by subtracting the results obtained in N₂-saturated KOH from those measured in O₂-saturated electrolyte to guarantee that only the current densities of phenomena related to the reduction of oxygen were represented. From this corrected LSV, different crucial ORR parameters were calculated: (i) the onset potential (E_{onset}) at a current density of 0.1 mA cm⁻² and (ii) the current density produced at 0.4 V vs RHE ($J_{0.4}$). The reaction mechanism was evaluated by using the current produced by the disk and ring of the RRDE, in which the ring potential was fixed at ca. 1.57 V vs RHE. These values can be used to calculate the formation of HO₂⁻ from a two-electron mechanism and the number of electrons exchanged (n_e) at each step of the reaction. Both were calculated with the currents obtained at 1600 rpm using Equations (2) and (3), respectively:

$$\text{HO}_2^- (\%) = 200 \times \frac{\frac{I_R}{N}}{I_D + \frac{I_R}{N}}, \quad (2)$$

$$n_e = \frac{4I_D}{I_D + \frac{I_R}{N}}, \quad (3)$$

where I_R is the ring current (mA), I_D is the disk current (mA), and N is the collection efficiency (0.249).

Moreover, the short-term performance (10,000 s) of each material toward ORR was determined by applying 0.4 V vs RHE. Additionally, the methanol tolerance of the best-performing sample and the commercial Pt/C were tested by the addition of 1.5 mL of methanol ($\geq 99.9\%$, VWR Chemicals, Radnor, PA, USA) to the electrolyte during chronoamperometric measurements at ca. 1000 s. Moreover, samples CG and CG/CNT_O were also analyzed by electrochemical impedance spectroscopy (EIS) with an AC amplitude of 10 mV and a frequency range from 1 MHz to 10 mHz using a fully discharged cell at 0 V.

3. Results and Discussion

3.1. Chemical Properties

Elemental and ICP-OES analyses were performed to determine the bulk composition of the electrocatalyst. The results obtained are detailed in Table 1.

Table 1. Chemical composition determined by elemental analysis and ICP-OES.

Sample	C [wt.%]	H [wt.%]	O [wt.%]	N [wt.%]	Fe [wt.%]
CG	90.8	1.7	7.5	-	-
CG/CNT _O	92.7	0.8	6.5	-	-
CG _{0.5Fe}	93.4	1.3	5.0	-	0.3
CG _{1Fe}	92.2	1.0	5.4	-	1.4
CG _{5Fe}	87.4	1.3	6.2	-	5.1
CG/CNT _{O,5Fe}	90.6	0.8	3.7	-	4.9
N-CG _{5Fe}	81.9	1.3	8.1	3.3	5.4
N-CG/CNT _{O,5Fe}	83.4	1.1	6.4	5.1	4.0
CG _{5Fe,N}	82.2	1.4	8.6	2.0	5.8
CG/CNT _{O,5Fe,N}	85.4	1.0	7.2	2.2	4.2

The carbonized hydrothermal samples (CG and CG/CNT_O) were primarily composed of carbon (Table 1), with some hydrogen and oxygen. The oxygen content decreases in the presence of oxidized CNTs, indicating that these CNTs favored the polymerization of glucose during the hydrothermal treatment [19,27]. Consequently, the hybrid materials have a lower amount of functional groups than their glucose-derived counterparts, as previously observed by Fourier transform infrared analysis [19]. On the other hand, the incorporation of iron onto CG and CG/CNT_O leads to a decrease in the relative oxygen content due to thermal treatment applied after the wetness impregnation with iron oxide. Nonetheless, increasing the amount of iron precursor during the impregnation process leads to an increase in the oxygen content due to the oxygen contribution of the Fe₂O₃ added that is not totally reduced in the final material, especially employing CG as support. Furthermore, interesting differences are observed regarding the oxygen content due to the incorporation of nitrogen. The addition of melamine to CG_{5Fe} and CG/CNT_{O,5Fe} leads to an increase in oxygen content from 6.2 wt.% and 3.7 wt.% to 8.6 wt.% (CG_{5Fe,N}) and 7.2 wt.% (CG/CNT_{O,5Fe,N}), respectively. Overall, the nitrogen functionalization of the carbon materials increases the oxygen content, whereas the methodology selected to incorporate Fe and N (a single-step or two-step process) does not seem to play an important role in the final oxygen content.

Regarding nitrogen content, the opposite effect is observed. In this case, the methodology employed to introduce N atoms to the carbons is crucial for the final relative content determined. The two-step methodology leads to a higher nitrogen bulk content of the carbon materials than a single-step process, which indicates that there are more possibilities for nitrogen bonding after the incorporation of iron due to the previous formation of stable species on the carbon matrix that will not compete with nitrogen upon the second

thermal treatment. Lastly, the iron content of Fe,N CGs and Fe,N CG/CNT_O is very similar within the same carbon support type (5.4 vs. 5.8 wt.% and 4.0 vs 4.2 wt.%, respectively). Nonetheless, it is possible to observe that the use of CG led to a slightly higher incorporation of iron atoms than CG/CNT_O. Furthermore, interesting differences in the chemical composition were also detected due to the synthesis process. Regardless of the doping method employed, the addition of CNTs during the hydrothermal polymerization results in hybrids that present lower oxygen and iron contents but higher nitrogen percentages than their non-hybrid counterparts (Table 1), which suggests that the presence of CNTs favors the preferential incorporation of nitrogen functionalities instead of iron oxide.

To fully understand the differences due to the methodologies employed for the Fe,N incorporation process, the surface composition of these four samples was determined by XPS. The survey spectra are presented in Figure S1, and their chemical surface compositions are detailed in Table S1. The XPS surveys indicate the presence of carbon, oxygen and nitrogen, but do not indicate the presence of iron on the materials' surface analyzed, which suggests that iron is probably incorporated inside the porous structure of the carbons instead of on the surface [36], which is confirmed by the ICP-OES analysis (Table 1). The surface chemical composition obtained by XPS follows the same trend as that obtained by elemental analysis. The presence of CNTs or the use of the two-step method for incorporation results in a higher nitrogen content (Table S1). To further understand the nitrogen bonds formed during the thermal treatments, the high-resolution XPS N 1s spectra of those samples prepared by the two-step method (N-CG_{5Fe} and N-CG/CNT_{O,5Fe}) and one-step method (CG_{5Fe,N} and CG/CNT_{O,5Fe,N}) were deconvoluted into the main four nitrogen functionalities (Figure 2): pyridinic nitrogen (N-6) at 398.3 ± 0.1 eV, pyrrolic nitrogen (N-5) at 400.2 ± 0.1 eV, quaternary nitrogen (N-Q) at 401.6 ± 0.1 eV, and oxidized nitrogen (N-X) at 404.1 ± 0.2 eV [37].

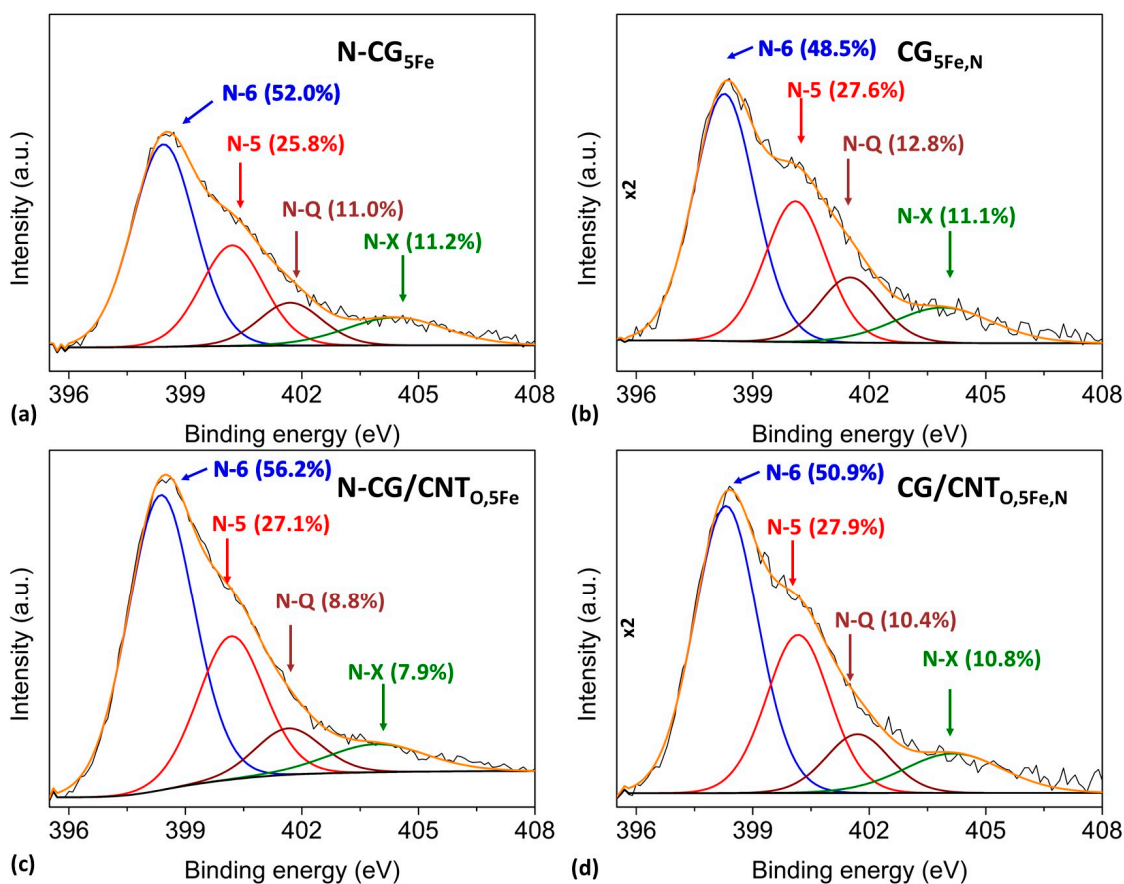


Figure 2. Deconvolution of the N 1s X-ray photoelectron spectra of N-CG_{5Fe} (a), CG_{5Fe,N} (b) N-CG/CNT_{O,5Fe} (c) and CG/CNT_{O,5Fe,N} (d) electrocatalysts.

Interesting differences are observed for the most common nitrogen functionalities. The relative composition of N-6 is higher in those materials in which the nitrogen precursor was treated under an inert atmosphere (N-CG_{5Fe} and N-CG/CNT_{O,5Fe}), while similar percentages of N-5 are observed in comparison with those samples treated under H₂ (CG_{5Fe,N} and CG/CNT_{O,5Fe,N}). Furthermore, the percentage of N-Q increases after the treatment under H₂ (Figure 2b,d). The increase in N-Q and decrease in N-6 may be an effect of the time used during the one-step method (4 h) in comparison to the two-step method (2 h), which favors the transformation of N-6 into N-Q [38,39]. Moreover, all N-doped samples present N-X groups, which indicates that oxygen bound to nitrogen during the thermal treatments, as melamine does not present oxygen in its composition. This is in agreement with the elemental analysis results that show an increase in the oxygen content upon incorporating nitrogen functionalities.

Nitrogen adsorption–desorption isotherms performed at $-196\text{ }^{\circ}\text{C}$ were used to evaluate the textural properties of the prepared carbons and are displayed in Figure S2a,b, whereas the pore size distribution obtained from these isotherms is presented in Figure S2c,d. The main textural parameters calculated from the isotherms are shown in Table 2.

Table 2. Textural properties determined by N₂ adsorption/desorption isotherms at $-196\text{ }^{\circ}\text{C}$.

Sample	S_{BET} (m ² g ⁻¹)	V_p (cm ³ g ⁻¹)	V_{micro} (cm ³ g ⁻¹)
CG	468	0.20	0.18
CG/CNT _O	418	0.27	0.15
CG _{0.5Fe}	549	0.22	0.21
CG _{1Fe}	517	0.21	0.19
CG _{5Fe}	530	0.22	0.20
CG/CNT _{O,5Fe}	441	0.31	0.16
N-CG _{5Fe}	396	0.18	0.14
N-CG/CNT _{O,5Fe}	59	0.12	0.01
CG _{5Fe,N}	440	0.19	0.16
CG/CNT _{O,5Fe,N}	316	0.26	0.11

Sample CG exhibits a type I isotherm characteristic of microporous materials [40]. Nonetheless, the presence of the oxidized CNTs modifies the isotherm to a type IV [40,41], with a type H3 hysteresis loop characteristic of slit-shaped pores [41,42]. Moreover, the hybrid obtained (CG/CNT_O) presents a slight decrease in microporosity, which may have been caused by the absence of microporosity in the CNTs. The incorporation of a 5 wt.% of iron led to an increase in the S_{BET} for both CG (from 468 to 530 m² g⁻¹) and CG/CNT_O (from 418 to 441 m² g⁻¹), as well as in the pore volume (from 0.20 to 0.22 cm³ g⁻¹ and 0.27 to 0.31 cm³ g⁻¹, respectively), which suggests that iron may be acting as an activating agent [43]. Regarding the pore size distribution, all of these samples are mainly composed of micropores (<2 nm) and some mesopores, which is in agreement with the hysteresis loop observed. The hybrid displays a slight shift of its pore widths to higher values than the CG sample (1.6 nm vs 1.5 nm, respectively) and a lower micropore volume (Figure S2c). The addition of iron leads to a slight decrease in the pore width, leading to micropores lower than 1 nm, and an overall increase in micropore volume for CG and hybrid samples. Regardless of the methodology employed to dope the carbons, Fe,N incorporation decreases the microporosity, especially in those samples prepared by the two-step method. This effect may be due to the time employed for the thermal treatments. In the two-step process, the melamine was only treated for 2 h under an N₂ atmosphere, while in the one-step process, the treatment took place for 2 h under N₂ and 2 h under H₂. This increase in residence time probably led to a higher degree of decomposition of the nitrogen precursor. The N-containing surface groups may have blocked some of the pores, thereby hindering the access of N₂ to the innermost pores during the isotherm measurements [20,36]. This is more evident for sample N-CG/CNT_{O,5Fe} which displayed the highest S_{BET} and microporosity

loss of all N-doped samples. This may be related to the higher nitrogen content of this sample in comparison to the other N-doped carbons synthesized, which increased the likelihood of having its pores blocked. This is also displayed in Figure S2d, in which sample N-CG/CNT_{O,5Fe} presents a very low micropore contribution ranging from 1.0 to 1.7 nm pore width. Moreover, the addition of melamine after the incorporation of iron (N-CG_{5Fe}) leads to a wider pore size distribution than the simultaneous incorporation of nitrogen and iron (CG_{5Fe,N}), which could indicate that some morphological differences may exist between these two processes.

The morphological changes that occur during both the hydrothermal processes and the subsequent incorporation of iron (5 wt.%) and nitrogen were observed by scanning electron microscopy (SEM). The corresponding micrographs are displayed in Figure 3.

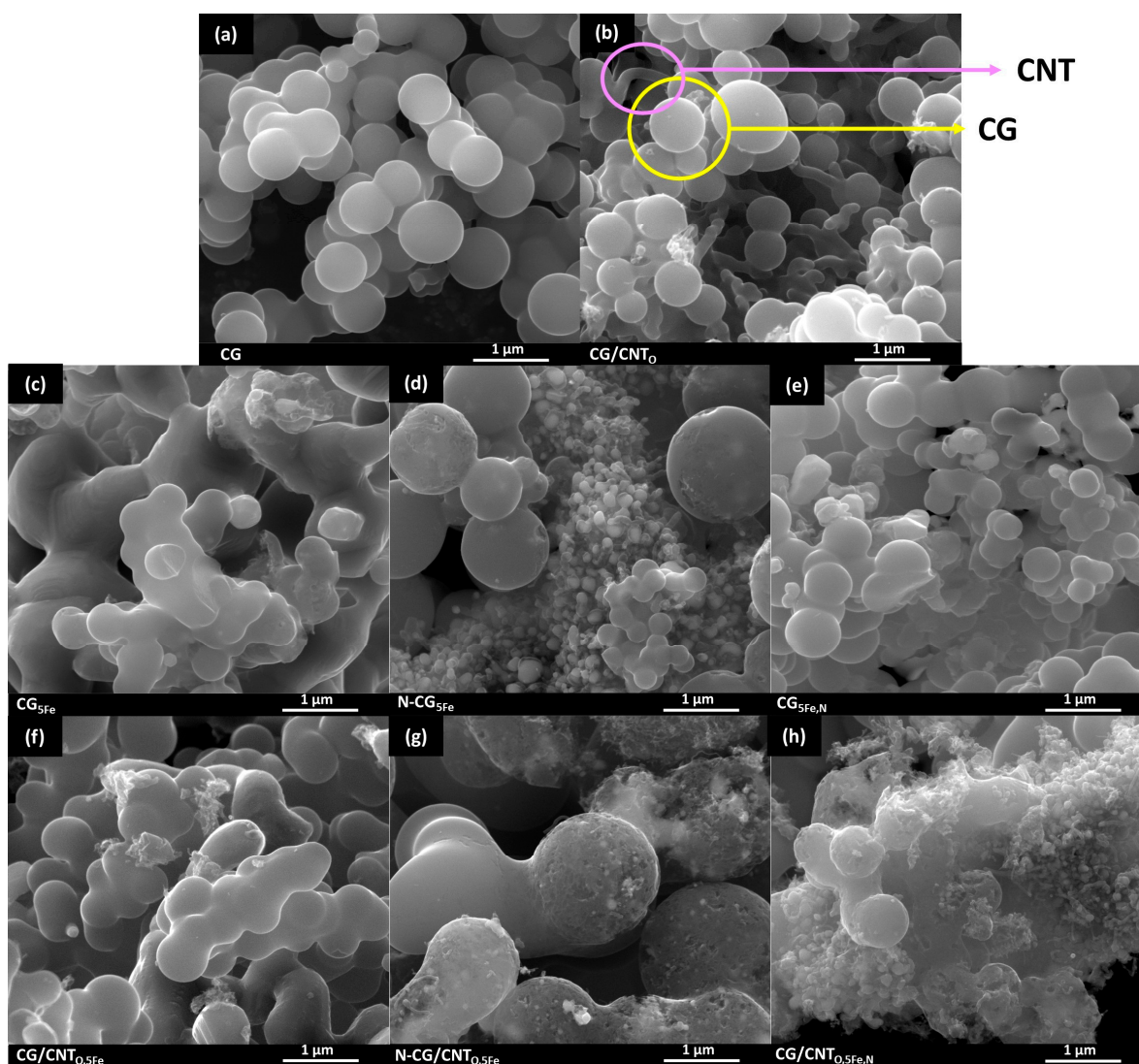


Figure 3. SEM micrographs of CG (a), CG/CNT_O (b), CG_{5Fe} (c), N-CG_{5Fe} (d), CG_{5Fe,N} (e), CG/CNT_{O,5Fe} (f), N-CG/CNT_{O,5Fe} (g) and CG/CNT_{O,5Fe,N} (h) electrocatalysts.

Sample CG is composed of spheres without defects (Figure 3a), which is a typical morphology of hydrothermal carbons [44,45]. The incorporation of CNT_O during hydrothermal polymerization leads to a combination of the carbon spheres and the CNTs, resulting in hybrid materials (Figure 3b). The addition of iron to the pristine samples (CG and CG/CNT_O) results in materials with interesting differences in their morphology. The micrographs of CG_{5Fe} (Figure 3c) and CG/CNT_{O,5Fe} (Figure 3f) exhibit some of the spheres

observed in the non-doped samples but also a large number of carbon spheres that have agglomerated into a single large cluster. The incorporation of nitrogen results in materials with different morphologies (Figure 3d,e,g,h) compared to those of the monometallic samples (Figure 3c,f), with the appearance of several defects on the surface of the spheres (Figure 3d,e,g,h), probably due to the formation of C-N bonds during the decomposition of the melamine. Moreover, sample N-CG_{5Fe} exhibits spheres with different sizes, which may contribute to a wider pore size distribution than the more homogeneous CG_{5Fe,N}. Additionally, the iron dispersion on the carbon materials, specifically in Fe,N hybrids (N-CG/CNT_{O,5Fe} and CG/CNT_{O,5Fe,N}), was analyzed by elemental mapping (Figure S3). The resulting micrographs indicate that iron is well dispersed in the area investigated, which indicates the successful incorporation of the metallic element across the carbon support.

To further address the changes attributed to the presence of CNT_O and/or the incorporation of iron and/or nitrogen, Raman spectroscopy was performed. The resulting spectra are exhibited in Figure S4. All carbons exhibit two main peaks: one associated with the carbon structure's basal plane defects (D band) at ca. 1350 cm⁻¹ and another peak attributed to the material's graphitic domains (G band) at ca. 1580 cm⁻¹. These two main bands were further deconvoluted to gain some insight into the number of defects of each material. The integration of the peak areas resulting from the deconvolution (A_D and A_G) was then used to calculate the A_D/A_G ratio (Table S2). As expected, the presence of CNT_O decreases the value of the A_D/A_G ratio in comparison to CG, due to the highly graphitic nature of the CNTs. The incorporation of iron does not significantly modify the structure of CG. However, the incorporation of 5 wt.% of iron into the CG/CNT_O hybrid results in a higher A_D/A_G ratio, which may be attributed to the anchoring of the precursor nanoparticles on the carbon structure, which leads to a more disordered matrix [46]. The incorporation of nitrogen by the two-step method (N-CG_{5Fe} and N-CG/CNT_{O,5Fe}) produces different variations depending on the pristine carbon (CG or CG/CNT_O). N-CG_{5Fe} presents a slightly lower A_D/A_G ratio (2.36) than CG (2.44) and CG_{5Fe} (2.41), which indicates that each step of the electrocatalyst preparation contributes to increasing the degree of order. Contrarily, N-CG/CNT_{O,5Fe} presents a higher A_D/A_G ratio (2.93) than both CG/CNT_O (2.22) and CG/CNT_{O,5Fe} (2.57), which indicates that the precursor added is generating defects in the structure [19]. On the other hand, the simultaneous incorporation of iron and nitrogen (CG_{5Fe,N} and CG/CNT_{O,5Fe,N}) results in a slight increase in the A_D/A_G ratio in comparison to their undoped counterparts (CG and CG/CNT_O, respectively) which indicates that the number of defects of the catalysts is increased during the incorporation process. These results indicate that the carbon support, precursors, and thermal treatments applied to synthesize these electrocatalysts are important parameters in the formation of defects.

3.2. Electrochemical Assessments

Oxygen Reduction Reaction

The synthesized electrocatalysts were initially screened toward the ORR by CV in a rotating ring-disk electrode (RRDE), using a scan rate range between 5 and 100 mV s⁻¹ in inert and O₂-saturated electrolyte without rotation. Measurements under an N₂-saturated medium (Figure S5) displayed featureless cyclic voltammograms, which indicate that no electrocatalytic activity took place under these conditions. However, CVs performed in O₂-saturated KOH (Figure S5) show well-defined cathodic peaks, which confirms the electroactivity of all electrocatalysts toward ORR. Nonetheless, electrochemical differences are observed between samples due to their physico-chemical properties; hence, the performance of all catalysts was assessed by LSV to correlate the electrochemical results and the properties of the materials. The LSVs of the electrocatalysts and Pt/C recorded in the O₂-saturated 0.1 mol L⁻¹ KOH electrolyte at 1600 rpm, and the respective number of electrons exchanged are plotted in Figure 4a,b and Figure 4c,d, respectively. The main electrochemical parameters obtained from the LSVs are exhibited in Table 3.

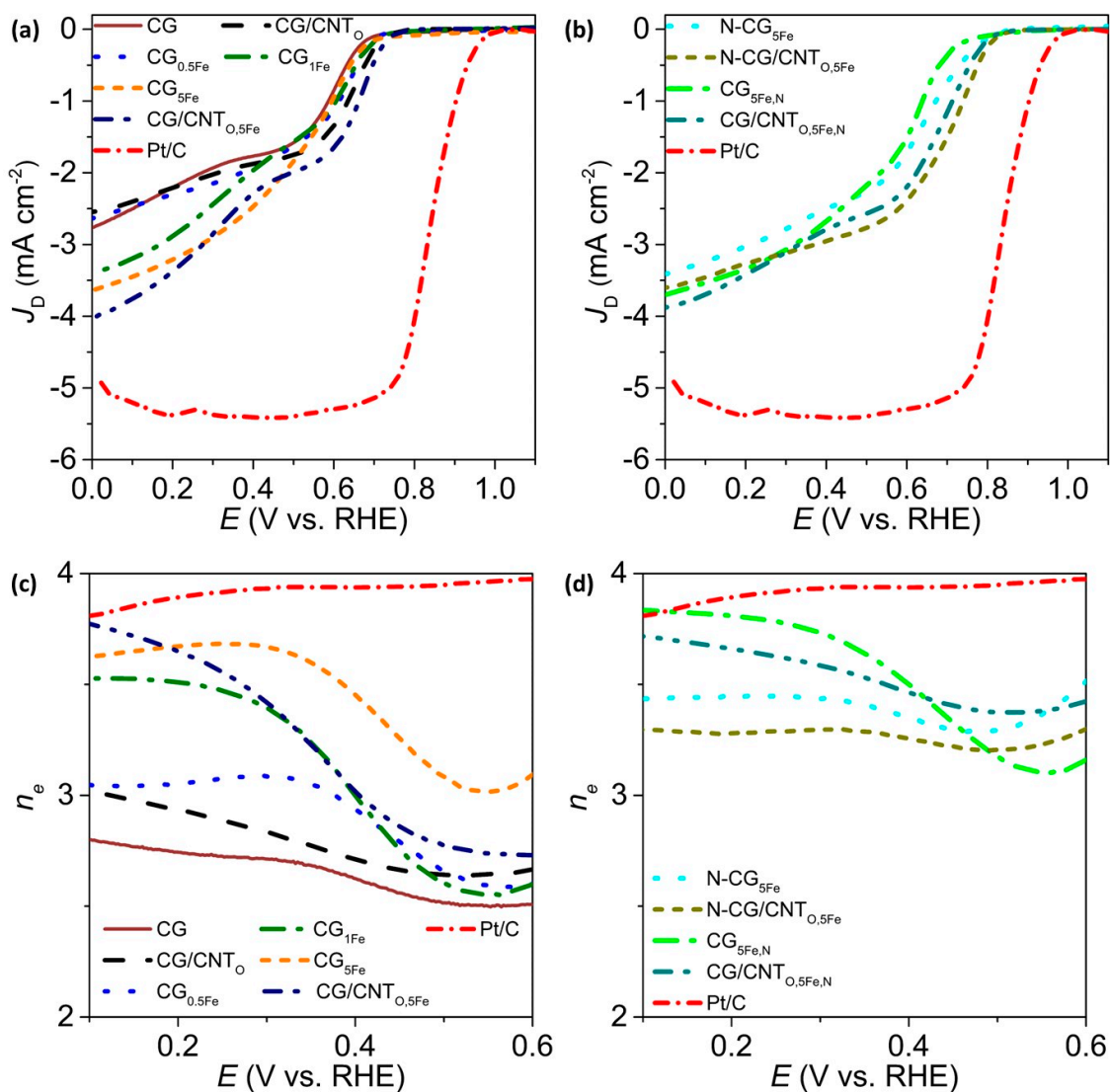


Figure 4. Disk current density produced by undoped and monometallic (a) and Fe,N (b) electrocatalysts at 1600 rpm in O₂-saturated electrolyte (0.1 mol L⁻¹ KOH) and number of electrons exchanged during the oxygen reduction reaction for undoped and monometallic (c) and Fe,N (d) electrocatalysts.

Table 3. Main electrochemical parameters: onset potential (E_{onset}), current density ($J_{0.4}$), hydrogen peroxide (HO₂⁻) formation, the number of electrons exchanged (n_e) and Tafel slope values for the synthesized materials and commercial Pt/C.

Sample	E_{onset} (V)	$J_{0.4}$ (mA cm ⁻²) ^a	HO ₂ ⁻ (%) ^a	n_e ^a	Tafel Slope (mV dec ⁻¹)
CG	0.70	1.77	69	2.6	117
CG/CNT _O	0.73	1.87	64	2.7	77
CG _{0.5Fe}	0.71	1.92	53	2.9	97
CG _{1Fe}	0.72	1.97	50	3.0	67
CG _{5Fe}	0.75	2.47	27	3.5	64
CG/CNT _{O,5Fe}	0.74	2.29	49	3.0	45
N-CG _{5Fe}	0.81	2.50	33	3.3	52
N-CG/CNT _{O,5Fe}	0.83	2.95	37	3.3	63
CG _{5Fe,N}	0.79	2.67	25	3.5	62
CG/CNT _{O,5Fe,N}	0.81	2.79	27	3.5	61
Pt/C	0.98	5.41	3	3.9	62

^a—Calculated at 0.4 V vs RHE.

The base CG and the hybrid CG/CNT_O were tested to evaluate their performance toward the ORR. The presence of CNT_O in the carbon structure shifts the E_{onset} by 30 mV from 0.70 V to 0.73 V, probably due to the higher number of active sites that were formed during the synthesis process. Furthermore, this hybrid exhibits an increase in $J_{0.4}$ of 6% and a small shift of the reaction mechanism from the two- to the four-electron pathway. These improvements are probably due to an increase in the electrical conductivity of the electrocatalyst [19]. To further investigate this hypothesis, electrochemical impedance spectroscopy (EIS) was performed on samples CG and CG/CNT_O at 0 V. The resultant Nyquist plots are displayed in Figure S6. These plots demonstrate that the presence of CNT_O led to a smaller semicircle, which indicates a decrease in the charge transfer resistance. This analysis suggests that the glucose/CNT hybrid has a higher electrical conductivity than the CG sample, which corroborates the previous statement. Furthermore, a decrease in the Tafel slope value from 117 mV dec⁻¹ (CG) to 77 mV dec⁻¹ (CG/CNT_O) is observed, which indicates a faster reaction rate [47].

The incorporation of different amounts of iron into the CG sample leads to an increase in E_{onset} and $J_{0.4}$. In fact, a direct relationship between these parameters and the amount of iron present in the electrocatalysts has been found (Figure S7). Furthermore, a decrease in the formation of HO₂⁻ and an increase in the number of electrons exchanged is also observed by increasing the percentage of iron. Similarly, the addition of 5 wt% of iron to the hybrid (CG/CNT_{O,5Fe}) increases the onset potential, current density, and number of electrons exchanged and decreases the formation of HO₂⁻. The incorporation of iron also decreases the Tafel slope value with increasing iron content from 97 mV dec⁻¹ (CG_{0.5Fe}) to 64 mV dec⁻¹ (CG_{5Fe}), which is comparable to the benchmark Pt/C at low overpotentials [47,48].

Regarding the incorporation of nitrogen, several interesting differences are observed in the ORR, which are probably correlated to the amount and type of functionalities present in each material. The incorporation of nitrogen increases the onset potential from 0.75 V (CG_{5Fe}) to 0.81 V (N-CG_{5Fe}) and 0.79 V (CG_{5Fe,N}), and from 0.74 V (CG/CNT_{O,5Fe}) to 0.83 V (N-CG/CNT_{O,5Fe}) and 0.81 V (CG/CNT_{O,5Fe,N}). The incorporation of nitrogen after iron (two-step method) results in a higher increase in the onset potential than the single-step method. This difference may be explained by the presence of larger amounts of N-6 in samples N-CG_{5Fe} and N-CG/CNT_{O,5Fe} than CG_{5Fe,N} and CG/CNT_{O,5Fe,N}, respectively, which is believed to govern the E_{onset} [49]. Regarding the current density of these four samples, very similar values are observed for all samples across the potentials applied. The very small differences observed in the LSVs (Figure 4b) may be due to the slightly different reaction mechanisms which gradually shift the LSV form from a two-plateau (two-electron mechanism) to a single plateau (four-electron mechanism) [20]. The use of a single-step functionalization leads to fewer side products and a larger number of electrons transferred than a two-step functionalization. This may be due to the higher amount of nitrogen incorporated by the latter which may be acting as an ORR active site and competing with iron, leading to a small shift in the reaction mechanism. Once again, the incorporation of CNT_O improves the E_{onset} but does not have any significant effect on the reaction mechanism, as N-CG/CNT_{O,5Fe} and CG/CNT_{O,5Fe,N} present the same values of HO₂⁻ and number of electrons transferred as their counterparts. Overall, N-6 functionalities increase the E_{onset} , whereas the number of N-Q groups favors a more direct reaction mechanism (four electrons) and decreases the formation of HO₂⁻. In comparison to similar N-doped carbons prepared using glucose as carbon source and melamine as nitrogen precursor [19], these materials (N-CG/CNT_{O,5Fe} and CG/CNT_{O,5Fe,N}) display a higher E_{onset} (0.83 V vs. 0.79 V vs. RHE), higher current density (3.0 mA cm⁻² vs. 2.5 mA cm⁻²), and a lower formation of HO₂⁻. All Fe,N carbon samples present a Tafel slope value close to 60 mV dec⁻¹, which indicates that the synthesized samples present a similar reaction rate to that of the Pt/C catalyst. Table S3 presents the ORR parameters of glucose-derived carbons published in the literature. Although the electrocatalytic activities obtained in this work are slightly inferior to those previously reported, it should be noted that the

methodologies employed and reagents used are more environmentally friendly than most of the presented literature results, without requiring the use of templates or complex procedures. Moreover, the reaction rate observed from the Tafel slope values demonstrates that the glucose/CNT hybrids display very similar kinetics to those of the benchmark catalysts and other glucose-derived electrocatalysts reported in the literature.

To further evaluate the performance of the electrocatalysts toward the ORR, another critical parameter was analyzed, namely the short-term stability. Therefore, chronoamperometry measurements were performed on all electrocatalysts by applying 0.4 V (vs RHE) for 10,000 s. The results obtained are exhibited in Figure 5.

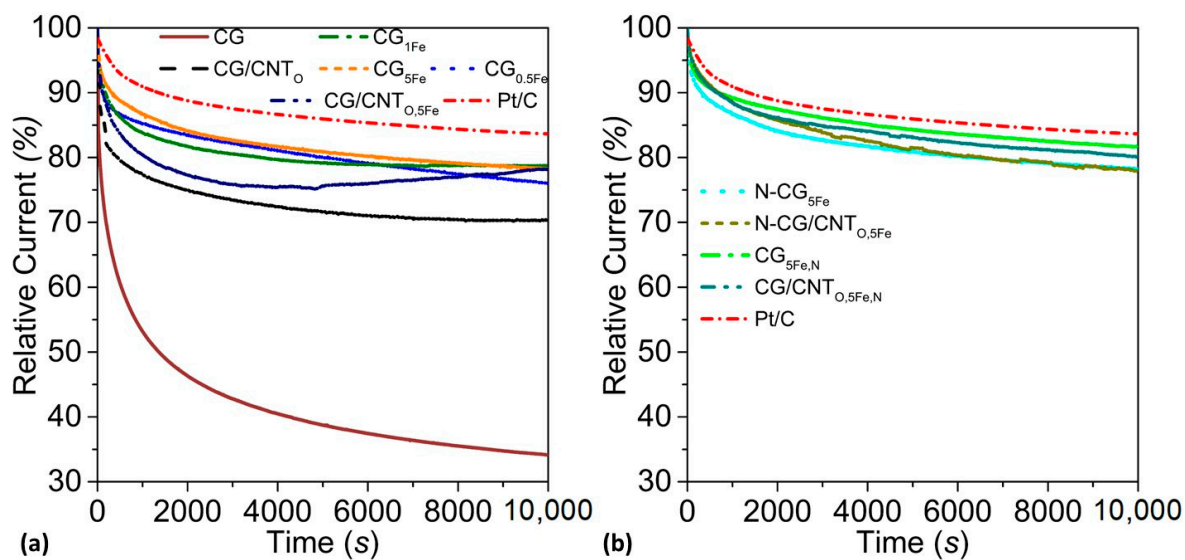


Figure 5. Chronoamperometry measurements (0.4 V for 10,000 s) for undoped and monometallic electrocatalysts (a), and Fe,N electrocatalysts (b) in an O₂-saturated 0.1 mol L⁻¹ KOH electrolyte at 1600 rpm.

CG exhibits very low short-term stability, losing 66% of its current density after 10,000 s, which is not ideal for upscale applications. The presence of CNT_O increases the current density retention of the electrocatalysts by 36%, which can be attributed to the higher performance stability of the CNTs [19] and the modification of the carbon properties during the synthesis. Nonetheless, this value is still not ideal for long-term applications. It should be noted that there is a large amount of HO₂⁻ formed with both electrocatalysts (Table 3), which may lead to the oxidation of the carbon surface [50–52], hindering their ability for O₂ adsorption and, consequently, their performance toward the ORR. The incorporation of iron leads to an increase in the catalysts' stability, as iron species act as the main active centers toward the ORR and highlight a lower degradation level in comparison to the undoped carbons. Furthermore, interesting differences are observed due to the methodology followed to incorporate iron and nitrogen. Samples prepared by incorporating iron and then nitrogen (two-step method) display the same stability as their monometallic counterparts. This indicates that even though different active centers are present on the carbon (nitrogen and iron), the overall degradation of these sites maintains the same level as the samples without nitrogen. On the other hand, samples prepared by the simultaneous incorporation of iron and nitrogen functionalities have higher stability, which may be due to the higher relative content of N-Q. These functional groups present strong bonds that may favor the retention of the current density and thus the better short-term application of these catalysts. Overall, the Fe,N samples using the single-step methodology (CG_{5Fe,N} and CG/CNT_{0.5Fe,N}) display very similar current density retentions (82% and 80%, respectively) in comparison to Pt/C (84%). Although the current density produced by these carbon electrocatalysts is still not on par with the

commercial catalyst, the short-term stability indicates that some positive aspects have already been developed and that further tailoring of the surface chemistry may lead to ORR performances similar to Pt/C. Samples CG/CNT_{0.5Fe,N} and Pt/C were then tested for methanol poisoning (Figure S8) by the addition of 1.5 mL of methanol to the electrolyte at ca. 1000 s of chronoamperometric measurements. These analyses demonstrated that the synthesized carbon material's electroactivity does not deteriorate with methanol poisoning, in contrast with Pt/C, confirming the potential of these materials toward the ORR in a methanol fuel cell. Due to the importance of CNTs in the performance of the hybrids, slightly increasing their amount during the hydrothermal process may lead to even higher electroactivities toward the ORR. Moreover, the incorporation of single atoms instead of using two different precursors may also improve the performance of the electrocatalysts and reduce their overall synthesis time and production costs. Therefore, the hybrids prepared in this work, although still underperforming compared to the Pt/C benchmark electrocatalyst, provide a good starting point for the development of green, sustainable, and cheap ORR electrocatalysts.

4. Conclusions

Carbon hybrids prepared by the hydrothermal treatment of glucose in the presence of oxidized CNTs were tailored by incorporating iron and/or nitrogen into their surface using two different methodologies: (i) the incorporation of iron followed by nitrogen doping and (ii) the simultaneous incorporation of the transition metal and the heteroatom in a single thermal treatment. The presence of CNT₀ favored the polymerization of glucose during the hydrothermal treatment, resulting in materials with a lower concentration of functional groups than their glucose-derived carbon counterparts. Nitrogen doping of the monometallic samples results in materials with a much higher concentration of nitrogen than the Fe,N samples prepared using a single thermal treatment. The use of aH₂ atmosphere during the thermal decomposition and longer residence time for the decomposition of melamine leads to lower contents of N-6 and higher amounts of N-Q. Regarding the electrochemical performance, E_{onset} increases by 130 mV in comparison to the carbonized glucose sample due to the presence of active centers such as iron and nitrogen functional groups, whereas the current density increases linearly with the iron content. The reaction mechanism shifts to a direct four-electron mechanism by the addition of nitrogen functionalities to the hybrid, which decreases the formation of HO₂⁻ to 25%. The short-term durability of the carbon hybrids is higher than that of the glucose-derived carbon and increases due to the incorporation of iron and N-Q moieties. Therefore, considering the overall ORR performance parameters, the Fe,N carbon hybrid prepared using the one-step method presents the highest short-term stability (80%) and lowest formation of HO₂⁻ (27%), whereas the hybrid prepared by the two-step method exhibits the highest onset potential (0.83 V) and current density (2.95 mA cm⁻²). Overall, Fe,N carbon hybrids present different advantages that may prove useful as a starting point to develop new electrocatalysts to replace the Pt/C benchmark.

Supplementary Materials: The following supporting information can be downloaded at: <https://www.mdpi.com/article/10.3390/c10020047/s1>, Figure S1: XPS survey spectra of the prepared Fe,N CG (a,b) and Fe,N CG/CNT hybrids (c,d) electrocatalysts, in which N-CG_{5Fe} and N-CG/CNT_{0.5Fe} were prepared using a two-step method and CG_{5Fe,N} and CG/CNT₀ were prepared using a one-step method; Table S1: Surface chemical composition determined by XPS; Figure S2: N₂ adsorption-desorption isotherms at -196 °C and pore size distribution of undoped, CG_{XFe} and CG/CNT_{0.5Fe} (a,c), and N-CG_{5Fe}, N-CG/CNT_{0.5Fe}, CG_{5Fe,N} and CG/CNT_{0.5Fe,N} (b,d) electrocatalysts; Figure S3: Elemental mapping of N-CG/CNT_{0.5Fe} (a) and CG/CNT_{0.5Fe,N} (b). Red—Carbon, Yellow—Iron, Green—Nitrogen, Blue—Oxygen; Figure S4: Raman spectra of undoped and monometallic electrocatalysts (a), and Fe,N electrocatalysts (b); Table S2: Ratio of the integrated D and G peaks obtained by Raman spectroscopy; Figure S5: Cyclic voltammograms recorded at 5 mV s⁻¹ in N₂- and O₂-saturated 0.1 mol L⁻¹ KOH electrolyte from 1.15 V to -0.05 V; Figure S6: Nyquist plots for CG and CG/CNT₀ obtained by electrochemical impedance spectroscopy at 0 V; Figure S7: Onset potential (a) and current

density at a potential of 0.4 V (b) obtained from the linear sweep voltammetry curves of Figure 5a (a) for the CG_{XFe} samples versus the percentage of Fe calculated by ICP; Table S3: ORR parameters of glucose-derived carbons, reagents and synthesis methods employed; Figure S8: Methanol tolerance of CG/CNT_{O,5Fe,N} and Pt/C at 0.4 V during 10,000 s.

Author Contributions: Conceptualization, N.R.-R., J.L.F. and M.F.R.P.; methodology, R.G.M. and N.R.-R.; validation, R.G.M.; writing—original draft preparation, R.G.M. and N.R.-R.; writing—review and editing, J.L.F. and M.F.R.P.; visualization, N.R.-R.; supervision, N.R.-R. and M.F.R.P.; funding acquisition, M.F.R.P. All authors have read and agreed to the published version of the manuscript.

Funding: This work is financially supported by national funds through the FCT/MCTES (PIDDAC), under the project Bicat4Energy, PTDC/EQU-EQU/1707/2020. This research was also funded by FCT/MCTES (PIDDAC): LSRE-LCM, UIDB/50020/2020 (<https://doi.org/10.54499/UIDB/50020/2020>) and UIDP/50020/2020 (<https://doi.org/10.54499/UIDP/50020/2020>); ALiCE, LA/P/0045/2020 (<https://doi.org/10.54499/LA/P/0045/2020>). RGM acknowledges the Research Grant from FCT 2020.06422.BD (<https://doi.org/10.54499/2020.06422.BD>).

Institutional Review Board Statement: Not applicable.

Informed Consent Statement: Not applicable.

Data Availability Statement: The raw data supporting the conclusions of this article will be made available by the authors on request.

Acknowledgments: The authors are indebted to CEMUP for assistance with SEM, BSED, EDS and elemental mapping analyses.

Conflicts of Interest: The authors declare no conflicts of interest.

References

- Kirubakaran, A.; Jain, S.; Nema, R. A review on fuel cell technologies and power electronic interface. *Renew. Sustain. Energy Rev.* **2009**, *13*, 2430–2440. [[CrossRef](#)]
- Stacy, J.; Regmi, Y.N.; Leonard, B.; Fan, M. The recent progress and future of oxygen reduction reaction catalysis: A review. *Renew. Sustain. Energy Rev.* **2017**, *69*, 401–414. [[CrossRef](#)]
- Goswami, C.; Hazarika, K.K.; Bharali, P. Transition metal oxide nanocatalysts for oxygen reduction reaction. *Mater. Sci. Energy Technol.* **2018**, *1*, 117–128. [[CrossRef](#)]
- Yang, J.; Toshimitsu, F.; Yang, Z.; Fujigaya, T.; Nakashima, N. Pristine carbon nanotube/iron phthalocyanine hybrids with a well-defined nanostructure show excellent efficiency and durability for the oxygen reduction reaction. *J. Mater. Chem. A* **2017**, *5*, 1184–1191. [[CrossRef](#)]
- Komba, N.; Zhang, G.; Wei, Q.; Yang, X.; Prakash, J.; Chenitz, R.; Rosei, F.; Sun, S. Iron (II) phthalocyanine/N-doped graphene: A highly efficient non-precious metal catalyst for oxygen reduction. *Int. J. Hydrogen Energy* **2019**, *44*, 18103–18114. [[CrossRef](#)]
- Hyun, K.; Ueno, T.; Panomsuwan, G.; Li, O.L.; Saito, N. Heterocarbon nanosheets incorporating iron phthalocyanine for oxygen reduction reaction in both alkaline and acidic media. *Phys. Chem. Chem. Phys.* **2016**, *18*, 10856–10863. [[CrossRef](#)]
- Han, S.; Hu, X.; Wang, J.; Fang, X.; Zhu, Y. Novel Route to Fe-Based Cathode as an Efficient Bifunctional Catalysts for Rechargeable Zn-Air Battery. *Adv. Energy Mater.* **2018**, *8*, 1800955. [[CrossRef](#)]
- Chung, H.T.; Cullen, D.A.; Higgins, D.; Sneed, B.T.; Holby, E.F.; More, K.L.; Zelenay, P. Direct atomic-level insight into the active sites of a high-performance PGM-free ORR catalyst. *Science* **2017**, *357*, 479–484. [[CrossRef](#)]
- Zhao, S.; Wang, D.; Amal, R.; Dai, L. Carbon-Based Metal-Free Catalysts for Key Reactions Involved in Energy Conversion and Storage. *Adv. Mater.* **2019**, *31*, e1801526.
- Figueiredo, J.L. Nanostructured porous carbons for electrochemical energy conversion and storage. *Surf. Coat. Technol.* **2018**, *350*, 307–312. [[CrossRef](#)]
- Wu, Z.; Song, M.; Wang, J.; Liu, X. Recent Progress in Nitrogen-Doped Metal-Free Electrocatalysts for Oxygen Reduction Reaction. *Catalysts* **2018**, *8*, 196. [[CrossRef](#)]
- Wang, J.; Wang, H.; Fan, Y. Techno-Economic Challenges of Fuel Cell Commercialization. *Engineering* **2018**, *4*, 352–360. [[CrossRef](#)]
- He, C.; Sankarasubramanian, S.; Matanovic, I.; Atanassov, P.; Ramani, V. Understanding the Oxygen Reduction Reaction Activity and Oxidative Stability of Pt Supported on Nb-Doped TiO₂. *ChemSusChem* **2019**, *12*, 3468–3480. [[CrossRef](#)]
- Li, Z.; Zhou, P.; Zhao, Y.; Jiang, W.; Zhao, B.; Chen, X.; Li, M. Ultradurable Pt-Based Catalysts for Oxygen Reduction Electrocatalysis. *Catalysts* **2024**, *14*, 57. [[CrossRef](#)]
- Lee, K.; Zhang, L.; Lui, H.; Hui, R.; Shi, Z.; Zhang, J. Oxygen reduction reaction (ORR) catalyzed by carbon-supported cobalt polypyrrole (Co-PPy/C) electrocatalysts. *Electrochim. Acta* **2009**, *54*, 4704–4711. [[CrossRef](#)]
- Paul, R.; Dai, Q.; Hu, C.; Dai, L. Ten years of carbon-based metal-free electrocatalysts. *Carbon Energy* **2019**, *2*, 151–152. [[CrossRef](#)]

17. Yan, L.; Yu, J.; Houston, J.; Flores, N.; Luo, H. Biomass derived porous nitrogen doped carbon for electrochemical devices. *Green Energy Environ.* **2017**, *2*, 84–99. [[CrossRef](#)]
18. Jain, A.; Balasubramanian, R.; Srinivasan, M.P. Hydrothermal conversion of biomass waste to activated carbon with high porosity: A review. *Chem. Eng. J.* **2016**, *283*, 789–805. [[CrossRef](#)]
19. Morais, R.G.; Rey-Raap, N.; Costa, R.S.; Pereira, C.; Guedes, A.; Figueiredo, J.L.; Pereira, M.F.R. Hydrothermal Carbon/Carbon Nanotube Composites as Electrocatalysts for the Oxygen Reduction Reaction. *J. Compos. Sci.* **2020**, *4*, 20. [[CrossRef](#)]
20. Morais, R.G.; Rey-Raap, N.; Figueiredo, J.L.; Pereira, M.F.R. Glucose-derived carbon materials with tailored properties as electrocatalysts for the oxygen reduction reaction. *Beilstein J. Nanotechnol.* **2019**, *10*, 1089–1102. [[CrossRef](#)]
21. John, K.I.; Omorogie, M.O. Biomass-based hydrothermal carbons for catalysis and environmental cleanup: A review. *Green Chem. Lett. Rev.* **2022**, *15*, 162–186. [[CrossRef](#)]
22. Skorupska, M.; Ilnicka, A.; Lukaszewicz, J.P. Successful Manufacturing Protocols of N-Rich Carbon Electrodes Ensuring High ORR Activity: A Review. *Processes* **2022**, *10*, 643. [[CrossRef](#)]
23. Sathiskumar, C.; Ramakrishnan, S.; Vinothkannan, M.; Kim, A.R.; Karthikeyan, S.; Yoo, D.J. Nitrogen-Doped Porous Carbon Derived from Biomass Used as Trifunctional Electrocatalyst toward Oxygen Reduction, Oxygen Evolution and Hydrogen Evolution Reactions. *Nanomaterials* **2020**, *10*, 76. [[CrossRef](#)]
24. Choi, E.Y.; Kim, D.E.; Lee, S.Y.; Kim, C.K. Electrocatalytic activity of nitrogen-doped holey carbon nanotubes in oxygen reduction and evolution reactions and their application in rechargeable zinc–air batteries. *Carbon* **2020**, *166*, 245–255. [[CrossRef](#)]
25. Liu, A.; Ma, M.; Zhang, X.; Ming, J.; Jiang, L.; Li, Y.; Zhang, Y.; Liu, S. A biomass derived nitrogen doped carbon fibers as efficient catalysts for the oxygen reduction reaction. *J. Electroanal. Chem.* **2018**, *824*, 60–66. [[CrossRef](#)]
26. Barrera, D.; Florent, M.; Kulko, M.; Bandosz, T.J. Ultramicropore-influenced mechanism of oxygen electroreduction on metal-free carbon catalysts. *J. Mater. Chem. A* **2019**, *7*, 27110–27123. [[CrossRef](#)]
27. Rey-Raap, N.; Enterría, M.; Martins, J.I.; Pereira, M.F.R.; Figueiredo, J.L. Influence of Multiwalled Carbon Nanotubes as Additives in Biomass-Derived Carbons for Supercapacitor Applications. *ACS Appl. Mater. Interfaces* **2019**, *11*, 6066–6077. [[CrossRef](#)]
28. Wang, W.; Jia, Q.; Mukerjee, S.; Chen, S. Recent Insights into the Oxygen-Reduction Electrocatalysis of Fe/N/C Materials. *ACS Catal.* **2019**, *9*, 10126–10141. [[CrossRef](#)]
29. Ma, Q.; Jin, H.; Zhu, J.; Li, Z.; Xu, H.; Liu, B.; Zhang, Z.; Ma, J.; Mu, S. Stabilizing Fe–N–C Catalysts as Model for Oxygen Reduction Reaction. *Adv. Sci.* **2021**, *8*, 2102209. [[CrossRef](#)]
30. Mamtani, K.; Jain, D.; Co, A.C.; Ozkan, U.S. Nitrogen-Coordinated Iron–Carbon as Efficient Bifunctional Electrocatalysts for the Oxygen Reduction and Oxygen Evolution Reactions in Acidic Media. *Energy Fuels* **2017**, *31*, 6541–6547. [[CrossRef](#)]
31. Yan, Z.; Dai, C.; Zhang, M.; Lv, X.; Zhao, X.; Xie, J. Nitrogen doped porous carbon with iron promotion for oxygen reduction reaction in alkaline and acidic media. *Int. J. Hydrogen Energy* **2019**, *44*, 4090–4101. [[CrossRef](#)]
32. Liu, Y.; Huang, B.; Zhang, X.; Huang, X.; Xie, Z. In-situ fabrication of nitrogen-doped carbon nanosheets containing highly dispersed single iron atoms for oxygen reduction reaction. *J. Power Sources* **2019**, *412*, 125–133. [[CrossRef](#)]
33. Abdelwahab, A.; Farghali, A.A.; Allah, A.E. Synergy between iron oxide sites and nitrogen-doped carbon xerogel/diamond matrix for boosting the oxygen reduction reaction. *Nanoscale Adv.* **2022**, *4*, 837–848. [[CrossRef](#)]
34. Xia, J.; Li, K.; Zhao, G.-L. Electric Field Polarization to Increase Bifunctional Oxygen Electrocatalyst Performance of Nitrogen–Iron Functionalized Carbon Nanomaterials. *ACS Appl. Energy Mater.* **2020**, *3*, 1484–1495. [[CrossRef](#)]
35. Canal-Rodríguez, M.; Rey-Raap, N.; Menéndez, J.Á.; Montes-Morán, M.A.; Figueiredo, J.L.; Pereira, M.F.R.; Arenillas, A. Effect of porous structure on doping and the catalytic performance of carbon xerogels towards the oxygen reduction reaction. *Micropor. Mesopor. Mater.* **2020**, *293*, 109811. [[CrossRef](#)]
36. Morais, R.; Rey-Raap, N.; Figueiredo, J.; Pereira, M. Highly electroactive N–Fe hydrothermal carbons and carbon nanotubes for the oxygen reduction reaction. *J. Energy Chem.* **2020**, *50*, 260–270. [[CrossRef](#)]
37. Ba, H.; Duong-Viet, C.; Liu, Y.; Nhut, J.-M.; Granger, P.; Ledoux, M.J.; Pham-Huu, C. Pham-Huu, Nitrogen-doped carbon nanotube spheres as metal-free catalysts for the partial oxidation of H₂S. *Comptes Rendus Chim.* **2016**, *19*, 1303–1309. [[CrossRef](#)]
38. Enterría, M.; Figueiredo, J.L. Nanostructured mesoporous carbons: Tuning texture and surface chemistry. *Carbon* **2016**, *108*, 79–102. [[CrossRef](#)]
39. Lai, L.; Potts, J.R.; Zhan, D.; Wang, L.; Poh, C.K.; Tang, C.; Gong, H.; Shen, Z.; Lin, J.; Ruoff, R.S. Exploration of the active center structure of nitrogen-doped graphene-based catalysts for oxygen reduction reaction. *Energy Environ. Sci.* **2012**, *5*, 7936–7942. [[CrossRef](#)]
40. Kecili, R.; Hussain, C.M. Chapter 4—Mechanism of Adsorption on Nanomaterials. In *Nanomaterials in Chromatography*; Hussain, C.M., Ed.; Elsevier: Amsterdam, The Netherlands, 2018; pp. 89–115.
41. Chang, S.-S.; Clair, B.; Ruelle, J.; Beauchêne, J.; Di Renzo, F.; Quignard, F.; Zhao, G.-J.; Yamamoto, H.; Gril, J. Mesoporosity as a new parameter for understanding tension stress generation in trees. *J. Exp. Bot.* **2009**, *60*, 3023–3030. [[CrossRef](#)]
42. Yurdakal, S.; Garlisi, C.; Özcan, L.; Bellardita, M.; Palmisano, G. Chapter 4—(Photo)catalyst Characterization Techniques: Adsorption Isotherms, SEM, FTIR, UV-VIS, Photoluminescence and Electrochemical Characterizations. In *Heterogeneous Photocatalysis*; Marci, G., Palmisano, L., Eds.; Elsevier: Amsterdam, The Netherlands, 2019; pp. 87–152.
43. Bedia, J.; Monsalvo, V.; Rodriguez, J.; Mohedano, A. Iron catalysts by chemical activation of sewage sludge with FeCl₃ for CWPO. *Chem. Eng. J.* **2017**, *318*, 224–230. [[CrossRef](#)]

44. Falco, C.; Marco-Lozar, J.; Salinas-Torres, D.; Morallón, E.; Cazorla-Amorós, D.; Titirici, M.; Lozano-Castelló, D. Tailoring the porosity of chemically activated hydrothermal carbons: Influence of the precursor and hydrothermal carbonization temperature. *Carbon* **2013**, *62*, 346–355. [[CrossRef](#)]
45. Sevilla, M.; Fuertes, A.B. Chemical and Structural Properties of Carbonaceous Products Obtained by Hydrothermal Carbonization of Saccharides. *Chem.-A Eur. J.* **2009**, *15*, 4195–4203. [[CrossRef](#)] [[PubMed](#)]
46. Xiao, L.; Schroeder, M.; Kluge, S.; Balducci, A.; Hagemann, U.; Schulz, C.; Wiggers, H. Direct self-assembly of Fe₂O₃/reduced graphene oxide nanocomposite for high-performance lithium-ion batteries. *J. Mater. Chem. A* **2015**, *3*, 11566–11574. [[CrossRef](#)]
47. Chen, W.; Xiang, Q.; Peng, T.; Song, C.; Shang, W.; Deng, T.; Wu, J. Reconsidering the Benchmarking Evaluation of Catalytic Activity in Oxygen Reduction Reaction. *iScience* **2020**, *23*, 101532. [[CrossRef](#)] [[PubMed](#)]
48. Shinagawa, T.; Garcia-Esparza, A.T.; Takanabe, K. Insight on Tafel slopes from a microkinetic analysis of aqueous electrocatalysis for energy conversion. *Sci. Rep.* **2015**, *5*, 13801. [[CrossRef](#)]
49. Ma, R.; Lin, G.; Zhou, Y.; Liu, Q.; Zhang, T.; Shan, G.; Yang, M.; Wang, J. A review of oxygen reduction mechanisms for metal-free carbon-based electrocatalysts. *NPJ Comput. Mater.* **2019**, *5*, 78. [[CrossRef](#)]
50. Peng, Y.; Liu, H. Effects of Oxidation by Hydrogen Peroxide on the Structures of Multiwalled Carbon Nanotubes. *Ind. Eng. Chem. Res.* **2006**, *45*, 6483–6488. [[CrossRef](#)]
51. Singh, H.; Zhuang, S.; Ingis, B.; Nunna, B.B.; Lee, E.S. Carbon-based catalysts for oxygen reduction reaction: A review on degradation mechanisms. *Carbon* **2019**, *151*, 160–174. [[CrossRef](#)]
52. Morais, R.; Rey-Raap, N.; Figueiredo, J.; Pereira, M. Fe, Co, N-doped carbon nanotubes as bifunctional oxygen electrocatalysts. *Appl. Surf. Sci.* **2022**, *572*, 151459. [[CrossRef](#)]

Disclaimer/Publisher's Note: The statements, opinions and data contained in all publications are solely those of the individual author(s) and contributor(s) and not of MDPI and/or the editor(s). MDPI and/or the editor(s) disclaim responsibility for any injury to people or property resulting from any ideas, methods, instructions or products referred to in the content.